

Article

Structural Analysis of Xylose Isomerase from *Streptomyces avermitilis*

Ki Hyun Nam 

College of General Education, Kookmin University, Seoul 02707, Republic of Korea; structure@kookmin.ac.kr

Abstract: Xylose isomerase (XI, also known as glucose isomerase) is an oxidoreductase that interconverts aldoses and ketoses. XI catalyzes the reversible isomerization of D-glucose and D-xylose into D-fructose and D-xylulose, respectively. The molecular function of XI is widely applied in producing high-fructose corn syrup (HFCS) in the food industry and bioethanol from hemicellulose in the biofuel industry. The structural information of XI from diverse strains is important for understanding molecular properties that can provide insights into protein engineering to improve enzyme efficiency. To extend the knowledge of the structural information on XI, the crystal structure of XI from *Streptomyces avermitilis* (SavXI) was determined at a 2.81 Å resolution. SavXI containing TIM barrel and extended α -helix domains formed the tetrameric assembly. The two metal-binding sites and their coordinating residues showed diverse conformations, providing the structural flexibility of the active site of SavXI. The structural comparison of SavXI and XI homologs exhibited unique metal-binding sites and conformations of the C-terminal α -helix domain. These structural results extend our knowledge of the molecular flexibility and mechanism of the XI family.

Keywords: xylose isomerase; glucose isomerase; metal-binding site; structure comparison; HFCS; bioethanol



Citation: Nam, K.H. Structural Analysis of Xylose Isomerase from *Streptomyces avermitilis*. *Crystals* **2024**, *14*, 446. <https://doi.org/10.3390/cryst14050446>

Academic Editors: Borislav Angelov and Neil Champness

Received: 4 April 2024

Revised: 23 April 2024

Accepted: 4 May 2024

Published: 7 May 2024



Copyright: © 2024 by the author. Licensee MDPI, Basel, Switzerland. This article is an open access article distributed under the terms and conditions of the Creative Commons Attribution (CC BY) license (<https://creativecommons.org/licenses/by/4.0/>).

1. Introduction

Xylose is naturally metabolized by several microorganisms, including bacteria, yeast, and fungi [1,2]. Xylose is consumed mainly through three metabolic pathways: the isomerase pathway; the oxidoreductase pathway; and the oxidative pathway, also recognized as the nonphosphorylative pathway [3]. The isomerase pathway is the first step in xylose metabolism in microbial cell physiology after the pentose phosphate cycle [4,5]. In this step, D-xylose is catalytically converted into D-xylulose by xylose isomerase (XI), indicating that XI is important in xylose utilization [6].

XI (also known as glucose isomerase; EC number 5.3.1.5) is an intramolecular oxidoreductase that interconverts aldoses and ketoses [7]. This induces a change in the position of carbonyl groups (C1 and C2) of the chemical structure between the substrate and the product [8]. The represented catalytic reaction of XI is the reversible conversion of D-glucose and D-xylose into D-fructose and D-xylulose, respectively. The XI enzyme also catalyzes the isomerization of L-arabinose into L-ribulose and generates the epimerization of D-xylose and L-arabinose into D-lyxose and L-ribose, respectively [5]. Although the conversion yield is not high, XI enables the conversion of L-rhamnose and D-allulose into L-rhamnulose and D-allose [9,10].

XI is a successful enzyme in various commercial industry applications, such as the food, biochemical, and biofuel fields [7]. In particular, XI is extensively used in the food and beverage industry to produce high-fructose corn syrup (HFCS), a fructose–glucose liquid sweetener alternative to sucrose [11–13]. Lignocellulosic biomass is the second major sugar found in most lignocellulosic hydrolysates and a major hemicellulose hydrolysate. The efficient utilization of carbon, such as xylose in lignocellulosic biomass, is economical and sustainable for biofuel and biochemical production [3,14,15]. XI is used in the biofuel

industry to produce bioethanol from hemicellulose [16]. To discover and utilize them more efficiently, functional studies are being conducted on new XIs from various strains, and structural studies are continuously being conducted to understand their molecular functions.

Streptomyces is the largest genus of the *Actinomycetota* class and is widely spread in various environments, such as extreme environments, underexplored habitats, terrestrial and marine regions, symbionts, and endophytes [17–19]. The *Streptomyces* genus is a rich source of secondary metabolites with various biological activities, medicinal chemicals, and novel drug leads [20,21]. This genus is also used as an industrial strain for producing commercial antibiotics, antifungals, therapeutics, and agricultural products [22]. In particular, the *Streptomyces* genus or XIs from *Streptomyces* are applied in the isomerization of sugar molecules. For example, *Streptomyces rubiginosus* exhibits isomerase activity in D-glucose, D-xylose, and L-arabinose [23]. *Streptomyces griseofuscus* S-41 shows isomerase activity in D-glucose, D-xylose, and D-ribose [24]. Commercially available XI from *Streptomyces murinus* exhibits isomerase activity for converting L-rhamnulose from L-rhamnose and D-allose from D-allulose [9].

Many successful cases of sugar conversion using these *Streptomyces* genus-derived XIs have been reported. Considering that >850 species from the *Streptomyces* genus have been reported [19,25,26], more valuable XIs from the *Streptomyces* genus can still be uncovered, which apply to valuable industries such as HFCS and bioethanol production. Studies on the engineering of XIs to improve enzyme activity in desired application environments are also being continuously conducted [27,28]. In contrast, the Protein Data Bank (PDB) has only reported the crystal structures of XI from six species of the *Streptomyces* genus, and structural information on strains belonging to the same genus, which differ in amino acid sequences from these, is limited. Accordingly, structural information, including molecular flexibility and conformational change, for new XIs can provide insights into the enzyme engineering of XIs for potential industrial applications.

Streptomyces avermitilis is a Gram-positive bacterium [29] and is a commercially important bacterial species used for the industrial production of avermectins, a family of broad-spectrum anthelmintic and insecticidal agents [30–32]. The XI gene encoded by *S. avermitilis* consists of 388 amino acids in protein databases. The molecular and structural functions of XI from *S. avermitilis* are unknown.

In this study, crystallographic studies of the crystal structure of XI from *S. avermitilis* at 2.81 Å resolution are reported. SavXI showed a tetrameric assembly in solution and crystal structure. It exhibited various conformational flexibilities at the metal-binding site in the active site. The structural similarities and differences in SavXI were compared with other XI structures. These results extend the knowledge of XI structures and provide insights into protein engineering for industrial applications.

2. Materials and Methods

2.1. Protein Preparation

The gene encoding XI from *S. avermitilis* (UniProt: Q93HF3; 388 amino acids) with an N-terminal thrombin cleavage site was codon-optimized for expression in *Escherichia coli* and synthesized (Bioneer, Daejeon, Republic of Korea). The synthesized gene was cloned into the pBT7-N-His vector (Bioneer). Recombinant DNA was transformed into *E. coli* BL21 (DE3) competent cells. The transformed cells were grown in 5 mL Luria–Bertani (LB) medium with 50 µg/mL of ampicillin on an orbital shaker at 200 rpm and 37 °C overnight. This culture was used to inoculate 2 L cultures of LB medium with 50 µg/mL ampicillin, which were grown with an orbital shaker at 180 rpm and 37 °C. When the OD₆₀₀ reached 0.8, protein expression was induced with 0.5 mM of isopropyl β-D-1-thiogalactopyranoside, and the culture was incubated at 18 °C overnight. Cells were harvested by centrifugation at 4000 rpm at 4 °C for 30 min. The cell pellet was resuspended in lysis buffer containing 50 mM of Tris-HCl (pH 8.0) and 200 mM of NaCl. The resuspended cells were lysed on ice using sonication. Cell debris was removed by centrifugation at 16,000 rpm at 4 °C.

The supernatant was filtered using a 0.45 µm syringe filter and applied to a Ni-NTA resin (Qiagen, Valencia, CA, USA) in a column. The resin was washed with 10 column volumes of wash buffer containing 50 mM of Tris-HCl (pH 8.0), 200 mM of NaCl, and 20 mM of imidazole. The protein was eluted with elution buffer containing 50 mM of Tris-HCl (pH 8.0), 200 mM of NaCl, and 300 mM of imidazole. Thrombin protease was added to the elution fraction to cleave the N-terminal His-tag and incubated at room temperature overnight. The protein was concentrated using a concentrator (Merck Millipore, Burlington, MA, USA; cutoff: 30 kDa) and loaded onto a HiPrep 16/60 Sephacryl S-200 HR column (GE Healthcare, Chicago, IL, USA) equilibrated with 10 mM of Tris-HCl (pH 8.0) and 200 mM of NaCl. The purity of the eluted protein solution was assessed using 12% sodium dodecyl sulfate–polyacrylamide gel electrophoresis (SDS-PAGE), and protein concentration was determined using the Bradford assay. The purified protein was concentrated to ~30 mg/mL for crystallization.

2.2. Crystallization

Crystallization screening was performed using the sitting drop vapor diffusion method at 20 °C using a commercial crystallization kit, including the Crystal Screen Kit, PEG/Ion, and Index (Hampton Research, Aliso Viejo, CA, USA). The protein solution (0.5 µL) was mixed with the crystallization screen solution (0.5 µL) and equilibrated with a reservoir solution (70 µL). Three different microcrystals were obtained from the following conditions: (i) Crystal Screen C12: 0.1 M of Tris-HCl (pH 8.5) and 8% (*w/v*) polyethylene glycol 8000; (ii) Index D10: 0.1 M of Bis-Tris (pH 6.5) and 20% (*w/v*) polyethylene glycol monomethyl ether 5000; and (iii) Index E10: 0.1 M of Bis-Tris (pH 6.5) and 45% (*v/v*) polypropylene glycol P400. Suitable crystals for X-ray diffraction were obtained from condition (i) within 5 months.

2.3. X-ray Diffraction Data Collection

X-ray diffraction data were collected at beamline 7A at Pohang Light Source II (PLS-II, Pohang, Republic of Korea) [33]. The SavXI crystal was cryoprotected using a reservoir solution supplemented with 25% (*v/v*) ethylene glycol for 5 s. The crystal was mounted on a goniometer under a 100 K nitrogen gas stream. Diffraction data were recorded on a Pilatus3 6M detector (DECTRIS, Baden, Switzerland), with a distance of 350 mm between the detector and the crystal. Diffraction data were indexed, integrated, and scaled using HKL2000 [34]. X-ray diffraction images were visualized using ADXV (<https://www.scripps.edu/tainer/arvai/adxv.html>, accessed on 18 August 2023).

2.4. Structure Determination

The phase problem was solved using molecular replacement, as implemented in MOLREP [35]. The crystal structure of glucose isomerase from *Streptomyces rubiginosus* (PDB code: 7DFJ) [36] was used as the search model. Manual model building based on an electron density map was performed with COOT [37]. Structure refinement was conducted with phenix.refine in PHENIX [38]. Structure validation was performed using MolProbity [38].

2.5. Bioinformatics and Structure Analysis

The tetrameric interface of SavXI was analyzed using the PDBePISA server [39]. Amino acid alignment was performed using Clustal Omega [40]. Structure-based multiple sequence alignment was visualized using ESPript 3.0 [41]. Protein structures were visualized with PyMOL (<https://pymol.org> (accessed on 8 March 2024)).

3. Results

3.1. Structure Determination

The codon-optimized SavXI gene for expression in *E. coli* cells was overexpressed in *E. coli* BL21 (DE3) with a high expression yield (>20 mg/L). The molecular mass of

SavXI was ~150 kDa on size exclusion chromatography, indicating the tetramer state in solution (Figure 1A). SavXI was crystallized in the following crystallization conditions: (i) Crystal Screen C12: 0.1 M of Tris-HCl (pH 8.5) and 8% (*w/v*) polyethylene glycol 8000; (ii) Index D10: 0.1 M of Bis-Tris (pH 6.5) and 20% (*w/v*) polyethylene glycol monomethyl ether 5000; and (iii) Index E10: 0.1 M of Bis-Tris (pH 6.5) and 45% (*v/v*) polypropylene glycol P400.

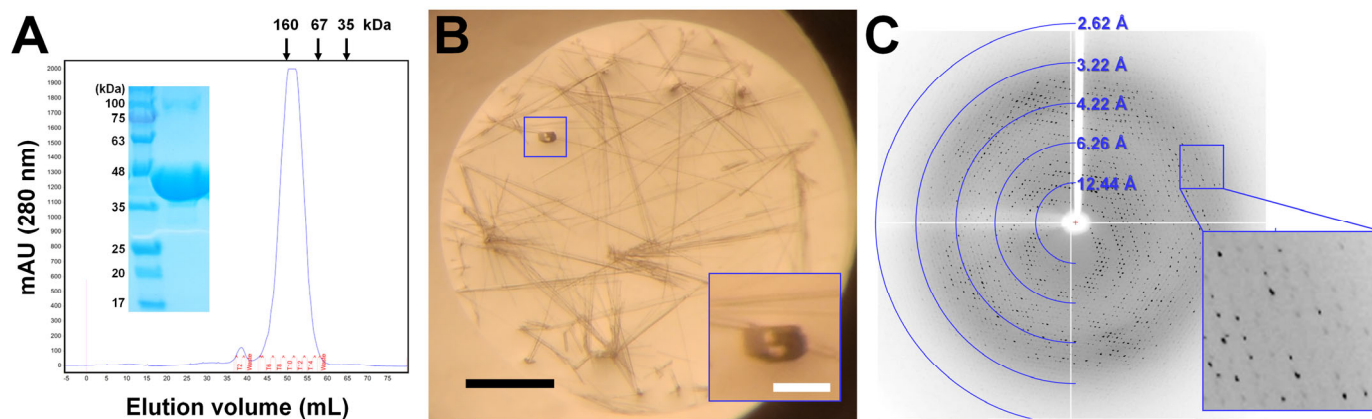


Figure 1. Purification, crystallization, and diffraction experiments of SavXI. (A) Gel filtration profile of SavXI indicating the tetrameric state. (Insert) Purity of SavXI on SDS-PAGE. (B) Photo of SavXI crystals grown under condition (i). Two different rod- and orthorhombic-shaped SavXI crystals are grown. Orthorhombic-shaped crystal (close-up view in the blue box) was used for the diffraction experiment. Black and white bars indicate 500 and 100 μm , respectively. (C) Diffraction pattern of SavXI from orthorhombic-shaped crystal.

In crystallization condition (i), two differently shaped SavXI crystals were grown (Figure 1B). Long rod-shaped SavXI crystals with dimensions of $<15 \times <15 \times >500 \mu\text{m}$ appeared within 1 month. This crystal form was grown reproducibly from other crystallization batches, but the crystal thickness was not increased. The diffraction experiment showed that long rod-shaped SavXI crystals were diffracted to $>20 \text{ \AA}$. Another SavXI crystal in the form of an orthorhombic appeared within 5 months, along with long rod-shaped SavXI crystals (Figure 1B). This crystal form was not reproducibly grown on the crystallization optimization experiment within 6 months. The orthorhombic SavXI crystal grown in the crystallization screen plate had crystal dimensions of $\sim 50 \times 50 \times 100 \mu\text{m}$. The diffraction experiment showed that the orthorhombic crystal form was diffracted up to $\sim 2.8 \text{ \AA}$ (Figure 1C); the crystal structure of SavXI was analyzed in this experiment. SavXI crystals grown under conditions (ii) and (iii) were cubic and cluster-shaped with a size of $<50 \mu\text{m}$ (Supplementary Figure S1). SavXI crystals were reproducibly grown under crystallization conditions (ii) and (iii). However, these SavXI crystals showed poor diffraction with diffraction up to $\sim 20 \text{ \AA}$.

3.2. Crystal Structure of SavXI

The SavXI crystal belonged to trigonal space group $P3_221$ with cell dimensions of $a = b = 129.13 \text{ \AA}$ and $c = 233.05 \text{ \AA}$ (Table 1). The SavXI structure was determined at a 2.81 \AA resolution with an R_{work} and R_{free} of 19.66 and 24.21, respectively.

Table 1. Data collection and refinement statistics for SavXI.

Data Collection	SavXI
X-ray source	7A beamline, PLS-II
Wavelength (Å)	0.9793
Space group	P3 ₂ 21
Cell dimension	
a, b, c (Å)	129.13, 129.13, 233.05
α, β, γ (°)	90.00, 90.00, 120.00
Resolution (Å)	50.0–2.80 (2.85–2.80)
Unique reflections	54,119 (2664)
Completeness (%)	97.8 (97.5)
Redundancy	6.4 (6.4)
I/σ	11.24 (2.1)
R _{merge}	0.262 (1.260)
R _{meas}	0.284 (1.360)
R _{pim}	0.107 (0.506)
CC1/2	0.977 (0.627)
CC*	0.994 (0.878)
Refinement	
Resolution (Å)	34.21–2.81
R _{work} ^a	0.1867
R _{free} ^b	0.2427
R.m.s. deviations	
Bonds (Å)	0.009
Angles (°)	1.136
B factors (Å ²)	
Protein	35.87
Metal ion	36.99
Ramachandran plot	
Favored (%)	94.66
Allowed (%)	4.77
Disallowed (%)	0.56

Values for the outer shell are noted in parentheses. ^a $R_{work} = \frac{\sum ||F_{obs}| - \sum |F_{calc}| |}{\sum |F_{obs}|}$, where F_{obs} and F_{calc} are the observed and calculated structure factor amplitudes, respectively. ^b R_{free} was calculated as R_{work} using a randomly selected subset of unique reflections not used for structural refinement.

Six SavXI molecules were occupied in an asymmetric unit. The electron density map of SavXI was well defined enough to build the model structure for all the residues (Asn2-Arg387). SavXI monomer had an N-terminal TIM barrel domain and a C-terminal extended α -helix domain (Figure 2A). The TIM barrel domain contained an active site pocket containing two metal-binding sites (M1 and M2) for the isomerization reaction. The C-terminal α -helix domain is involved in intermolecular contacts between the subunits that make up the tetramer [42]. This monomeric SavXI formed the tetrameric assembly with 222 symmetry (Figure 2B). In the asymmetric unit, four molecules exhibited a tetrameric formation, and the other two molecules also formed a tetrameric formation with two symmetric molecules in the crystal lattice (Supplementary Figure S2). In the tetrameric assembly of SavXI, the TIM barrel domains of Molecules A and B (C and D) interacted, creating an active site pocket. The C-terminal extended α -helix domains of Molecules A and B (C and D) interacted with the surrounding TIM barrel domain in a tetrameric formation (Figure 2B). In the tetrameric formation of SavXI, the solvent-accessible area of Molecules A to D was $\sim 19,160 \text{ \AA}^2$. At the interface between Molecules A and B, there were 120 amino acids. A total of 24.43% of Molecule A ($\sim 4657 \text{ \AA}^2$)'s surface was buried in interface A–B. Interface A–B was stabilized by 57 hydrogen bonds and 30 salt bridge interactions between Molecules A and B (Supplementary Table S1). The solvation energy gain in complex formation and the average gain of Molecule A were -22.3 and -10.4 kcal/mol, respectively. At the interface between Molecules A and C, there were 46 amino acids. A total

of 7.9% of Molecule A ($\sim 1521 \text{ \AA}$)'s surface was buried in interface A–C. Interface A–C was stabilized by 26 hydrogen bonds and 16 salt bridge interactions between Molecules A and C (Supplementary Table S2). The solvation energy gain in complex formation and the average gain of Molecule A were -2.6 and -3.5 kcal/mol, respectively. At the interface between Molecules A and D, there were 40 amino acids. A total of 7.4% of Molecule A ($\sim 1425 \text{ \AA}$)'s surface was buried in interface A–D. Interface A–D was stabilized by 18 hydrogen bonds and nine salt bridge interactions between Molecules A and D (Supplementary Table S3). The solvation energy gain in complex formation and the average gain of Molecule A were -2.4 and -3.4 kcal/mol, respectively. Taken together, numerous amino acids were involved in the tetrameric formation of SavXI, which was stabilized by hydrogen bond and salt bridge interactions.

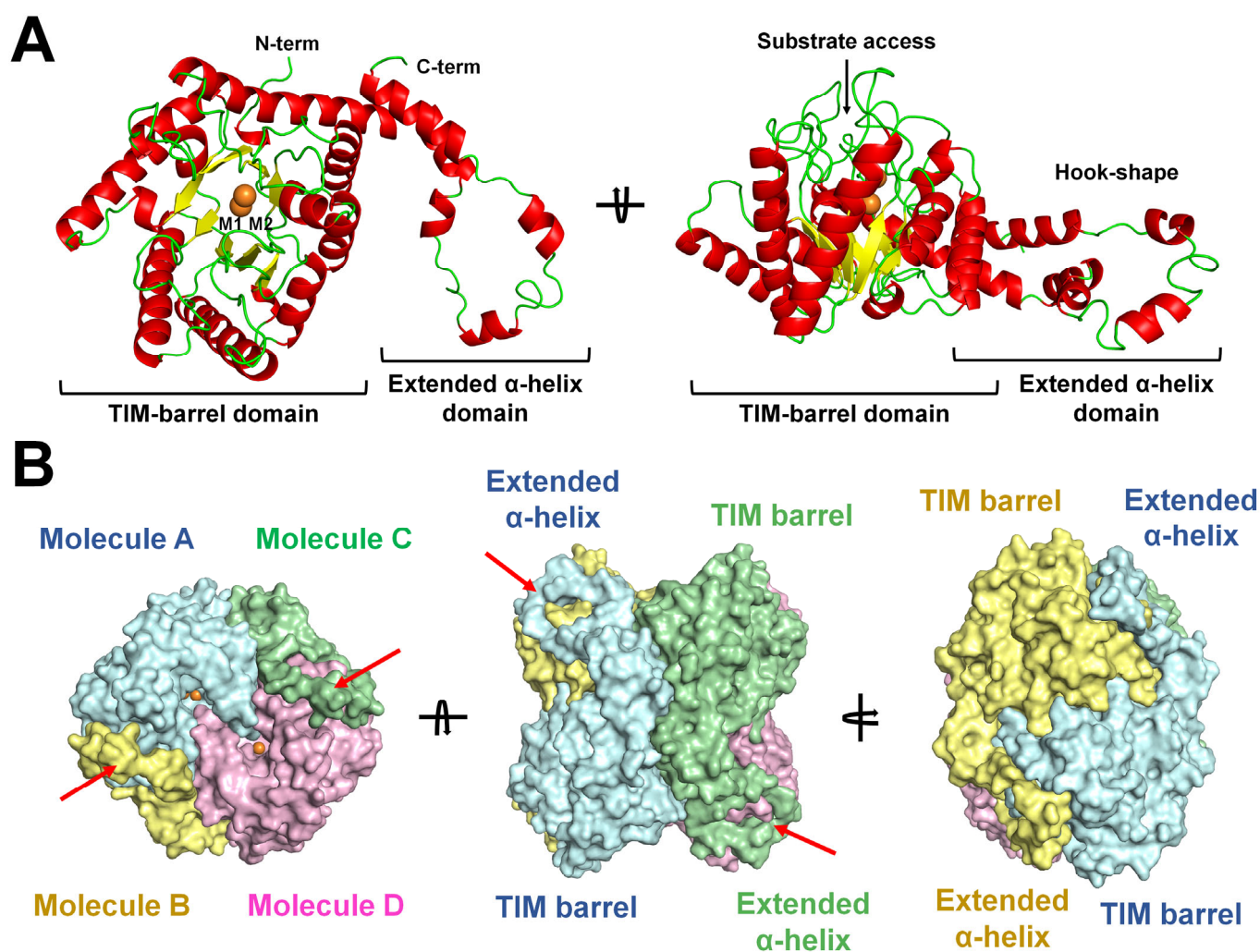


Figure 2. Crystal structure of SavXI. (A) Cartoon representation of monomeric SavXI. The TIM barrel domain contains the active site pocket, with two metal-binding sites indicated by spheres. (B) Tetrameric formation of SavXI. The metal ions in the active site pocket are indicated by spheres. The hook-shaped C-terminal α -helix domain interacting with the TIM barrel domain of the neighboring molecule is indicated by red arrows.

3.3. Active Site of SavXI

The active site containing two metal-binding sites was located on the TIM barrel domain. The loop between the $\alpha 1$ - and $\alpha 2$ -helices on the TIM barrel domain from the neighboring molecule was located at the substrate access entrance on the TIM barrel domain (Figure 3A). Consequently, the two TIM barrel domains had their own active sites

containing metal binding sites, and each TIM barrel domain contributes to the formation of substrate entry channels for a neighboring molecule. The distance from the metal-binding sites to the substrate-binding entrance in SavXI was ~ 15 Å (Figure 3B). B-factor analysis revealed that the loops (Thr91-Val98 and Trp137-Glu141) on the substrate-binding entrance of the TIM barrel domain exhibited a rigid conformation, with an average B-factor of 32.84 Å². In contrast, the $\alpha 1$ - $\alpha 2$ loop (Arg23-Asp28) showed relatively high flexibility with an average B-factor value of 41.41 Å². The average dimensions of the substrate-binding channel entrance were $\sim 6 \times 8$ Å (Figure 3A), indicating that sugar molecules such as xylose or glucose can access it, but large sugar molecules may not reach the substrate-binding site. During structure refinement, two strong positive peaks ($>5 \sigma$) were observed in a Fo-Fc electron density map corresponding to the known metal-binding sites on the active site of SavXI (Figure 3C), indicating that the purified recombinant SavXI contains metal ions at conserved metal-binding sites among the XI family, without adding divalent metal ions. The two metal-binding sites (M1 and M2) were coordinated by conserved metal-binding residues Glu181, Glu217, His220, Asp245, Asp255, Asp257, and Asp287. These metal-binding residues in SavXI are absolutely conserved within the XI family. The XI family required divalent cations such as Mg^{2+} , Mn^{2+} , or Co^{2+} for the isomerization reaction [43,44]. Class I XI family members, to which SavXI belongs, are known to prefer Mg^{2+} -binding at metal binding sites. When Mg^{2+} was modeled into two metal-binding sites of SavXI, no negative Fo-Fc electron density maps were observed on the M1 and M2 sites. The B-factor values of the M1/M2 sites modeled with Mg^{2+} from Molecules A, B, C, D, E, and F were $38.47/40.01$, $38.90/36.75$, $37.07/35.33$, $35.68/33.05$, $32.37/44.22$, and $29.43/42.56$ Å², respectively, indicating that there is no trend for the B-factor between the M1 and M2 sites. The average B-factor values of Mg^{2+} at the M1 and M2 sites were 35.32 and 38.65 Å², respectively, similar to the B-factor value of the protein of 35.87 Å². Absolutely conserved His and Lys residues are located around the metal-binding site of the XI family, which are involved in substrate opening [45] and isomerization reactions [46], respectively. In the substrate-binding channel of SavXI, the same absolute conserved His54 and Lys183 residues exist, and they are located 6.93 and 4.68 Å away from the M1 and M2 sites, respectively.

The M1 site was coordinated by Glu181, Glu217, Asp245, and Asp287 at distances (averaged from six molecules from the asymmetric unit) of 1.94 , 2.26 , 2.60 , and 1.94 Å, respectively (Figure 3D and Supplementary Table S4). A positive Fo-Fc electron density map was observed at the M1 site, which located the direction of the substrate-binding channel (Supplementary Figure S3). The shapes of these electron density maps from the six molecules in the asymmetric unit varied, indicating that some ligands may bind to the M1 site nonspecifically (see Discussion). The coordination angles of Glu181-M1-Asp245, Glu181-M1-Glu217, Asp245-M1-Asp287, and Glu217-M1-Asp287 were 96.1° , 87.06° , 91.2° , and 87.11° , respectively (Figure 3E and Supplementary Table S5). The M2 site was coordinated by Glu217, His220, Asp255, and Asp257 at distances of 2.31 , 2.85 , 2.31 , and 2.83 Å, respectively (Figure 3D and Supplementary Table S4). The average coordination angles of Glu217-M2-His220, Glu217-M2-Asp287, His220-M2-Asp255, and Asp255-M2-Asp257 were 68.01° , 70.65° , 82.01° , and 72.31° , respectively (Figure 3E and Supplementary Table S5). Taken together, the metal-binding distance of the M1 site was shorter than that of M2, indicating that the M1 site interacts with the metal more tightly than the M2 site. Moreover, in terms of geometry angle, the M1 site maintained coordination that was more stable than the M2 site. The superimposition of the two metal-binding sites on the active site from six SavXI molecules showed that the positions of the M1 and M2 sites and the conformation of the metal-interacting residues are variable (Figure 3F).

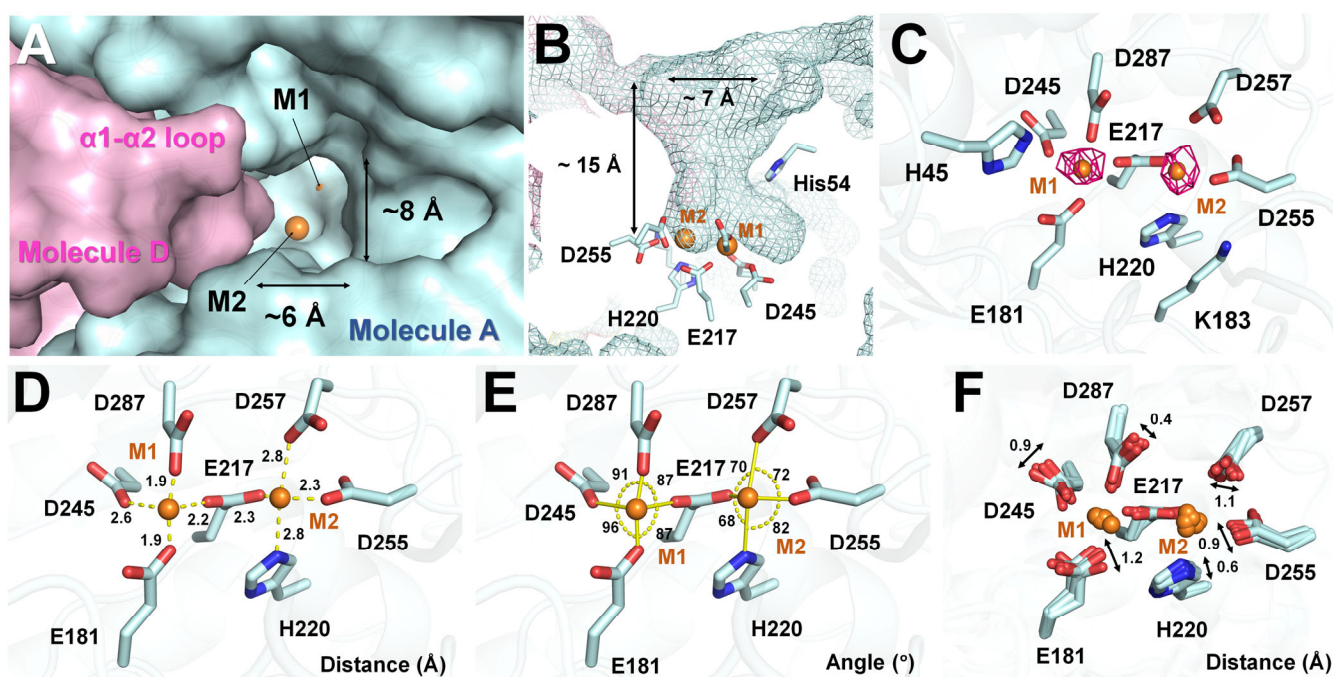


Figure 3. Active site of SavXI. (A) Substrate entrance of SavXI formed by the assembly of two TIM barrel domains. The $\alpha 1$ - $\alpha 2$ loop from Molecule D contributes to the formation of the substrate entrance channel of Molecule A. (B) Side view of the substrate-binding pocket of SavXI. The surface including the substrate binding channel is indicated by mesh. (C) Fo-Fc omit electron density map (magenta mesh, 5.0σ) for the metal-binding site on the active site of SavXI. (D) Interactions of M1 and M2 sites with interacting conserved residues of SavXI. (E) Geometries of M1 and M2 sites with their interacting residues for SavXI. (F) Superimposition of metal-binding sites of six SavXI molecules from the asymmetric unit.

3.4. Structural Comparison of SavXI with Other XI Structures

To investigate whether SavXI has unique structural properties, the crystal structure of SavXI was compared with other XI structures deposited in the PDB. The XI family can be divided into class I (~390 amino acids) and class II based on amino acid length, with class II XIs having an N-terminal extension of 40 to 50 amino acids [43]. SavXI belongs to the class I XI family and was compared with other class I XIs from various strains, including *Streptomyces albus* (SalXI; PDB code: 6XIA), *Streptomyces diastaticus* (SdiXI; 1CLK), *S. murinus* (SmuXI; 1DXI), *Streptomyces olivochromogenes* (SolXI; 1XYC), *Streptomyces* sp. F-1 (SspXI1; 6N99), *Streptomyces* sp. F-1 (SspXI2; 6N98), *Streptomyces* sp. SK (Ssp3XI; 4HHL), *S. rubiginosus* (SruXI; 5I7G), *Arthrobacter* sp. (AspXI; 1DID), *Actinoplanes missouriensis* (AmiXI; 1BHW), *Thermus caldophilus* (TcaXI; 1BXC), and *Thermus thermophilus* HB8 (TthXI; 1BxB). SavXI exhibited high amino acid sequence similarity with SalXI (sequence identity: 91.8% in 388 residues), SdiXI (90.7%/388), SmuXI (94.6%/388), SolXI (95.3%/387), SspXI1 (94.8%/388), SspXI3 (93.6%/388), and SruXI (92.5%/388), whereas SavXI had low sequence similarity with SspXI2 (68.1%/386) (Supplementary Figure S4 and Figure 4A). These results indicated that amino acid sequences among XIs within the *Streptomyces* genus may vary.

All these XI homologs shared the N-terminal TIM barrel and C-terminal α -helix domains, but distinct conformations were observed. The superimposition of SavXI with XI structures from *Streptomyces* species showed that the $C\alpha$ positions of SavXI were similar to those of SalXI (r.m.s. deviation: $0.328 \text{ \AA}/376$ atoms), SdiXI ($0.321/346$), SolXI ($0.321/358$), SspXI1 ($0.404/377$), SspXI3 ($0.296/352$), and SruXI ($0.328/377$) (Supplementary Figure S5). These results indicate that SavXI is structurally similar to SalXI, SdiXI, SmuXI, SolXI, SspXI1, SspXI3, and SruXI. However, these structures exhibit slight differences in the conformation of the metal-binding sites and metal-binding states, and they also show slight differences in

molecular flexibility (Supplementary Figures S6 and S7). The main chain conformation of the C-terminal helix domain of SavXI differed from that of SmuXI (0.426/362) and SspXI2 (0.456/321) (Figure 4B,C). The structural difference between the C-terminal α -helix domains of SavXI and SmuXI was caused by a change in the conformation of the side chain of Asp345. In SavXI, the side chain of Asp345 was inside a hook-shaped region of the C-terminal α -helix domain (Figure 4B). Conversely, in SmuXI, the side chain of Asp345 faced outward in a hook-shaped region of the C-terminal α -helix domain, indicating that structural changes in the C-terminal helix domain may vary even if the amino acid sequence is the same. In SspXI2, the low amino acid sequence similarity with SavXI caused different structural properties (Supplementary Figure S4 and Figure 4A). Superimposed structures showed that the main chain position and the conformation of the C-terminal α -helix domain between SavXI and SspXI2 are different (Figure 4C). Accordingly, distinct structural properties of the C-terminal α -helix domain will have different effects on the structural stability of the XI tetrameric formation.

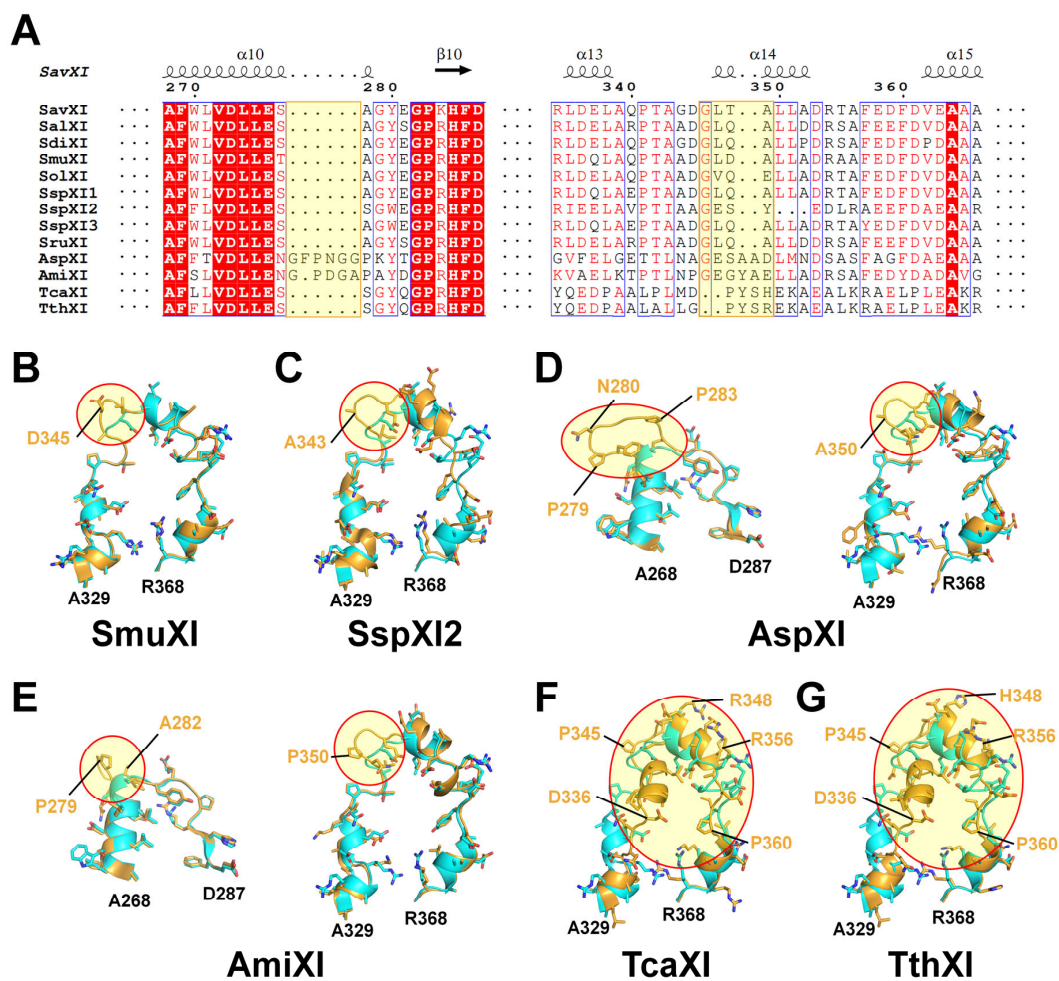


Figure 4. Amino acid and structure comparison of SavXI with other class XI proteins. (A) Partial amino acid sequence alignment of SavXI (UniProt: Q93HF3) with *S. albus* (P24299), *S. diastaticus* (P50910), *S. murinus* (P37031), *S. olivochromogenes* (P15587), *Streptomyces* sp. F-1 (A0A1K2FKX8), *Streptomyces* sp. F-1 (A0A1K2FZ20), *Streptomyces* sp. SK (Q9ZAI3), *S. rubiginosus* (P24300), *Arthrobacter* sp. strain NRRL B3728 (P12070), *A. missouriensis* (P12851), *T. caldophilus* (P56681), and *T. thermophilus* HB8 (P26997). Structure comparison of SavXI (cyan) with (B) SmuXI (PDB code: 1DXI), (C) SspXI2 (6N98), (D) AspXI (1DID), (E) AmiXI (1BHW), (F) TcaXI (1BXC), and (G) TthXI (1BXB).

For other species, SavXI had relatively low amino acid sequence similarity with AspXI (63.0% identity in 395 residues), AmiXI (66.8%/394), TcaXI (57.5%/386), and TthXI

(58.3%/386) (Supplementary Figure S4 and Figure 4A). The structure comparison of SavXI with AspXI (r.m.s. deviation: 0.478/333 atoms) and AmiXI (0.486/346) revealed two different structural features for the loop between the α 10-helix and β 10-strand and the C-terminal extended α -helix (Figure 4D,E). The different structural features of the α 10- β 10 loop of SavXI compared with AspXI and AmiXI were caused by the insertion of six amino acids in AspXI and AmiXI (Figure 4A,D,E). These inserted amino acid regions were located on the surface of the tetrameric AspXI and AmiXI, indicating that these regions may mainly affect XI solubility. The different structural feature of the C-terminal extended α -helix domain of SavXI compared with AspXI and AmiXI was also caused by the insertion of two amino acids in AspXI and AmiXI (Figure 4A,D,E), which may affect the affinity of the tetramer assembly. Significant conformational differences in the C-terminal extended α -helix domain of SavXI were observed when compared with TcaXI (0.668/0.332) and TthXI (0.701/337) (Figure 4F,G). Although the amino acid length of the C-terminal region of SavXI was the same as that of TcaXI and TthXI, the sequence identity was low (Figure 4A). These distinct conformations of the C-terminal region of TcaXI and TthXI caused different structural properties for the tetrameric assembly. These different conformations of the C-terminal hook-shaped region have been suggested to affect the tight tetrameric structure [47].

4. Discussion

Xylose (glucose) isomerase is an essential enzyme for microbial metabolism utilizing xylose and is also an important enzyme in producing HFCS and bioenergy. In this study, the crystal structure of XI from *S. avermitilis* was reported for the first time, providing structural information for potential XI utilization and enzyme engineering.

The codon-optimized SavXI gene for *E. coli* expression was overexpressed, confirming its use in industrial applications. Two strong positive peaks ($>5\sigma$) were observed in a Fo-Fc electron density map corresponding to the known metal-binding sites of the recombinant SavXI, indicating that the metal ions at the active site of SavXI may have been spontaneously acquired during protein expression in *E. coli* or protein purification. General XI exhibited enzyme activity in the presence of Mg^{2+} , Mn^{2+} , or Co^{2+} [43,44]. During model building, Mg^{2+} was modeled at the metal-binding site of SavXI due to its common preference in class I XIs. The average B-factor value of the metal-binding sites was reasonable compared with the B-factor value of the protein. However, it was still unclear which metal ions were bound or preferred in SavXI. Therefore, identifying metal ions at the active site of SavXI will be necessary to understand the exact molecular function. In particular, the nature of the metal ions can be established by methods such as inductively coupled plasma mass spectrometry or inductively coupled plasma atomic emission spectrometry from the protein in solution. Moreover, identifying the optimal metal ions for the isomerization reaction will also be required for future industrial applications of SavXI.

The interaction distance and coordinating geometry of the conserved metal-binding residues interacting with metal ions at M1 and M2 sites varied. This could be due to the occupancy of metal ions at the metal site of SavXI or the influence of the molecule bound to the M1 site of SavXI. First, when the metal ion does not completely occupy the metal-binding site of SavXI, the conformation of metal-binding residues may vary depending on the ratio of metal ion occupancy at the metal-binding site. Second, an ambiguous positive Fo-Fc electron density map was observed at the M1 site of SavXI (Supplementary Figure S3), which can affect the metal-binding site. The crystal structure of glucose isomerase from *Streptomyces rubiginosus* (SruGI) showed that molecules such as water or glycerol derived from cryoprotectant solutions bound to the M1 site [48]. However, the electron density map observed at the M1 site of SavXI differed from that of water or reagents used during crystallization or data collection. Based on the ambiguous shape of the electron density map, it was presumed that potentially heterogeneous molecules were interacting with the M1 site of SavXI. In the crystal structure of SruGI complexed with xylitol, xylitol bound to the M1 site affected the coordination of the metal-ion-binding site at M1 and M2 and

the release of the metal ion at the M2 site [36,49]. The heterogeneous molecules bound to the M1 site of SavXI affected the various conformations of the metal-binding M1 and M2 sites along with metal ion occupancy. Accordingly, to analyze the geometry of the metal-binding site of SavXI more accurately, it is necessary to chelate uncertain metal ions in the recombinant SavXI, followed by soaking the metal ions involved in the activity and determining their high-resolution structure.

The substrate-binding pocket of SavXI was formed by two TIM barrel domains from the tetrameric assembly. The substrate entrance was narrowed by the α 1- α 2 loop from the neighbor TIM barrel domain in tetrameric SavXI. B-factor analysis revealed relatively low flexibility in the loops at the entrance of the TIM barrel, whereas the α 1- α 2 loop, crucial for determining the dimension of the substrate entrance, exhibited relatively high flexibility. The previous subatomic resolution structure of SruGI complexed with xylitol showed that xylitol inhibitor bound to the M1 site induced the rearrangement of amino acids coordinating the M1 and M2 sites and a conformational change in the substrate-binding channel, including the α 1- α 2 loop [49]. Considering the high similarity in amino acid sequence and protein structure between SavXI and SruGI, the structure of the substrate-binding entrance of SavXI may influence molecular conformation and flexibility upon substrate binding.

In summary, despite various XIs from *Streptomyces* being present in the protein database, most have not undergone an analysis of their biological functions or structural characterization. The structural analysis of SavXI presented here will offer valuable structural information for the utilization and protein engineering of *Streptomyces*-derived XIs. However, structural analysis of SavXI has been conducted using a medium-resolution structure; therefore, high-resolution crystallization is necessary in future studies to obtain more accurate structural information. To provide more valuable information, future biochemical studies of SavXI and the determination of its high-resolution structure with homogeneous or functional metal ion binding will be crucial for further understanding its function and application development.

Supplementary Materials: The following supporting information can be downloaded at <https://www.mdpi.com/article/10.3390/cryst14050446/s1>: Figure S1. Photo of SavXI crystals grown under conditions (ii) and (iii). Figure S2. SavXI molecules in the asymmetric unit. Figure S3. Unidentified electron density maps at the M1 site of SavXI. Figure S4. Structure-based amino acid sequence alignment of SavXI with other XIs. Figure S5. Superimposition of SavXI with other XIs. Figure S6. Superimposition of the metal-binding site of SavXI with other XIs. Figure S7. B-factor putty representation of SavXI with other XIs. Table S1. Interaction between Molecules A and B. Table S2. Interaction between Molecules A and C. Table S3. Interaction between Molecules A and D. Table S4. Distance between metal-binding sites and key residues. Table S5. Coordination angle for metal-binding sites.

Funding: This work was funded by the National Research Foundation of Korea (NRF) (NRF-2021R1I1A1A01050838).

Data Availability Statement: Coordinates and structure factor amplitudes for both structures have been deposited in the PDB under the accession code 8YUD (<https://www.rcsb.org/structure/8YUD>).

Acknowledgments: I would like to thank the beamline staff at the 7A beamline at the Pohang Accelerator Laboratory for their assistance with data collection.

Conflicts of Interest: The author declares no conflicts of interest.

References

1. Zhao, Z.; Xian, M.; Liu, M.; Zhao, G. Biochemical routes for uptake and conversion of xylose by microorganisms. *Biotechnol. Biofuels* **2020**, *13*, 21. [[CrossRef](#)] [[PubMed](#)]
2. Bhosale, S.H.; Rao, M.B.; Deshpande, V.V. Molecular and industrial aspects of glucose isomerase. *Microbiol. Rev.* **1996**, *60*, 280–300. [[CrossRef](#)] [[PubMed](#)]
3. Domingues, R.; Bondar, M.; Palolo, I.; Queirós, O.; de Almeida, C.D.; Cesário, M.T. Xylose Metabolism in Bacteria—Opportunities and Challenges towards Efficient Lignocellulosic Biomass-Based Biorefineries. *Appl. Sci.* **2021**, *11*, 8112. [[CrossRef](#)]

4. Chang, C.; Park, B.C.; Lee, D.-S.; Suh, S.W. Crystal structures of thermostable xylose isomerases from *Thermus caldophilus* and *Thermus thermophilus*: Possible structural determinants of thermostability. *J. Mol. Biol.* **1999**, *288*, 623–634. [[CrossRef](#)] [[PubMed](#)]
5. Singh, P.; Kumar, S. Microbial Enzyme in Food Biotechnology. In *Enzymes in Food Biotechnology*; Academic Press: Cambridge, MA, USA, 2019; pp. 19–28.
6. Chu, L.; Zan, X.; Tang, X.; Zhao, L.; Chen, H.; Chen, Y.Q.; Chen, W.; Song, Y. The role of a xylose isomerase pathway in the conversion of xylose to lipid in *Mucor circinelloides*. *RSC Adv.* **2016**, *6*, 77944–77952. [[CrossRef](#)]
7. Nam, K.H. Glucose Isomerase: Functions, Structures, and Applications. *Appl. Sci.* **2022**, *12*, 428. [[CrossRef](#)]
8. Jänis, J.; Pasanen, S.; Rouvinen, J.; Vainiotalo, P. Characterization of the pH-dependent dissociation of a multimeric metalloprotein *Streptomyces rubiginosus* xylose isomerase by ESI FT-ICR mass spectrometry. *J. Mass Spectrom.* **2008**, *43*, 1376–1380. [[CrossRef](#)] [[PubMed](#)]
9. Choi, M.N.; Shin, K.-C.; Kim, D.W.; Kim, B.-J.; Park, C.-S.; Yeom, S.-J.; Kim, Y.-S. Production of D-Allose From D-Allulose Using Commercial Immobilized Glucose Isomerase. *Front. Bioeng. Biotechnol.* **2021**, *9*, 681253. [[CrossRef](#)] [[PubMed](#)]
10. Kim, Y.-S.; Kim, D.-Y.; Park, C.-S. Production of l-rhamnulose, a rare sugar, from l-rhamnose using commercial immobilized glucose isomerase. *Biocatal. Biotransformation* **2017**, *36*, 417–421. [[CrossRef](#)]
11. Jin, L.Q.; Xu, Q.; Liu, Z.Q.; Jia, D.X.; Liao, C.J.; Chen, D.S.; Zheng, Y.G. Immobilization of Recombinant Glucose Isomerase for Efficient Production of High Fructose Corn Syrup. *Appl. Biochem. Biotechnol.* **2017**, *183*, 293–306. [[CrossRef](#)]
12. Visuri, K.; Klibanov, A.M. Enzymatic production of high fructose corn syrup (HFCS) containing 55% fructose in aqueous ethanol. *Biotechnol. Bioeng.* **2004**, *30*, 917–920. [[CrossRef](#)]
13. White, J.S. Straight talk about high-fructose corn syrup: What it is and what it ain't. *Am. J. Clin. Nutr.* **2008**, *88*, 1716S–1721S. [[CrossRef](#)]
14. Alper, H.; Stephanopoulos, G. Engineering for biofuels: Exploiting innate microbial capacity or importing biosynthetic potential? *Nat. Rev. Microbiol.* **2009**, *7*, 715–723. [[CrossRef](#)] [[PubMed](#)]
15. Van Vleet, J.H.; Jeffries, T.W. Yeast metabolic engineering for hemicellulosic ethanol production. *Curr. Opin. Biotechnol.* **2009**, *20*, 300–306. [[CrossRef](#)] [[PubMed](#)]
16. Singh, R.S.; Singh, T.; Pandey, A. Microbial Enzymes—An Overview. In *Advances in Enzyme Technology*; Elsevier: Amsterdam, The Netherlands, 2019; pp. 1–40.
17. Khadayat, K.; Sherpa, D.D.; Malla, K.P.; Shrestha, S.; Rana, N.; Marasini, B.P.; Khanal, S.; Rayamajhee, B.; Bhattarai, B.R.; Parajuli, N. Molecular Identification and Antimicrobial Potential of *Streptomyces* Species from Nepalese Soil. *Int. J. Microbiol.* **2020**, *2020*, 8817467. [[CrossRef](#)]
18. Lee, N.; Hwang, S.; Kim, J.; Cho, S.; Palsson, B.; Cho, B.-K. Mini review: Genome mining approaches for the identification of secondary metabolite biosynthetic gene clusters in *Streptomyces*. *Comput. Struct. Biotechnol. J.* **2020**, *18*, 1548–1556. [[CrossRef](#)] [[PubMed](#)]
19. Alam, K.; Mazumder, A.; Sikdar, S.; Zhao, Y.-M.; Hao, J.; Song, C.; Wang, Y.; Sarkar, R.; Islam, S.; Zhang, Y.; et al. *Streptomyces*: The biofactory of secondary metabolites. *Front. Microbiol.* **2022**, *13*, 968053. [[CrossRef](#)]
20. Omura, S.; Ikeda, H.; Ishikawa, J.; Hanamoto, A.; Takahashi, C.; Shinose, M.; Takahashi, Y.; Horikawa, H.; Nakazawa, H.; Osonoe, T.; et al. Genome sequence of an industrial microorganism *Streptomyces avermitilis*: Deducing the ability of producing secondary metabolites. *Proc. Natl. Acad. Sci. USA* **2001**, *98*, 12215–12220. [[CrossRef](#)]
21. Lacey, H.J.; Rutledge, P.J. Recently Discovered Secondary Metabolites from *Streptomyces* Species. *Molecules* **2022**, *27*, 887. [[CrossRef](#)]
22. Noguchi, Y.; Kashiwagi, N.; Uzura, A.; Ogino, C.; Kondo, A.; Ikeda, H.; Sota, M. Development of a strictly regulated xylose-induced expression system in *Streptomyces*. *Microb. Cell Fact.* **2018**, *17*, 151. [[CrossRef](#)]
23. Langan, P.; Sangha, A.K.; Wymore, T.; Parks, J.M.; Yang, Z.K.; Hanson, B.L.; Fisher, Z.; Mason, S.A.; Blakeley, M.P.; Forsyth, V.T.; et al. L-Arabinose binding, isomerization, and epimerization by D-xylose isomerase: X-ray/neutron crystallographic and molecular simulation study. *Structure* **2014**, *22*, 1287–1300. [[CrossRef](#)]
24. Kasumi, T.; Hayashi, K.; Tsumura, N. Purification and Enzymatic Properties of Glucose Isomerase from *Streptomyces griseofuscus*, S-41. *Agric. Biol. Chem.* **2014**, *45*, 619–627. [[CrossRef](#)]
25. Kemung, H.M.; Tan, L.T.-H.; Khan, T.M.; Chan, K.-G.; Pusparajah, P.; Goh, B.-H.; Lee, L.-H. *Streptomyces* as a Prominent Resource of Future Anti-MRSA Drugs. *Front. Microbiol.* **2018**, *9*, 2221. [[CrossRef](#)] [[PubMed](#)]
26. Aryal, S.; Neupane, L.; Adhikari, R.; Regmi, B.; Koirala, N.; Joshi, D.R. Novel *Streptomyces* Sp. Reported in 2018: A Meta-Analysis. *Anti-Infect. Agents* **2021**, *19*, 3–14. [[CrossRef](#)]
27. Karimaki, J.; Parkkinen, T.; Santa, H.; Pastinen, O.; Leisola, M.; Rouvinen, J.; Turunen, O. Engineering the substrate specificity of xylose isomerase. *Protein Eng. Des. Sel.* **2005**, *17*, 861–869. [[CrossRef](#)]
28. Lee, M.; Rozeboom, H.J.; Keuning, E.; de Waal, P.; Janssen, D.B. Structure-based directed evolution improves *S. cerevisiae* growth on xylose by influencing in vivo enzyme performance. *Biotechnol. Biofuels* **2020**, *13*, 5. [[CrossRef](#)] [[PubMed](#)]
29. Burg, R.W.; Miller, B.M.; Baker, E.E.; Birnbaum, J.; Currie, S.A.; Hartman, R.; Kong, Y.-L.; Monaghan, R.L.; Olson, G.; Putter, I.; et al. Avermectins, New Family of Potent Anthelmintic Agents: Producing Organism and Fermentation. *Antimicrob. Agents Chemother.* **1979**, *15*, 361–367. [[CrossRef](#)] [[PubMed](#)]
30. He, B.; Guo, J.; Zhang, X.; Chen, Z.; Wen, Y.; Li, J. Two Adjacent and Similar TetR Family Transcriptional Regulator Genes, SAV577 and SAV576, Co-Regulate Avermectin Production in *Streptomyces avermitilis*. *PLoS ONE* **2014**, *9*, e99224. [[CrossRef](#)] [[PubMed](#)]

31. Liu, W.; Zhang, Q.; Guo, J.; Chen, Z.; Li, J.; Wen, Y.; Elliot, M.A. Increasing Avermectin Production in *Streptomyces avermitilis* by Manipulating the Expression of a Novel TetR-Family Regulator and Its Target Gene Product. *Appl. Environ. Microbiol.* **2015**, *81*, 5157–5173. [[CrossRef](#)] [[PubMed](#)]
32. Horii, S.; Samuel, A.Z.; Nakashima, T.; Take, A.; Matsumoto, A.; Takahashi, Y.; Ando, M.; Takeyama, H. Mycelial differentiation linked avermectin production in *Streptomyces avermitilis* studied with Raman imaging. *Appl. Microbiol. Biotechnol.* **2022**, *107*, 369–378. [[CrossRef](#)]
33. Park, S.Y.; Ha, S.C.; Kim, Y.G. The Protein Crystallography Beamlines at the Pohang Light Source II. *Biodesign* **2017**, *5*, 30–34.
34. Otwinowski, Z.; Minor, W. Processing of X-ray diffraction data collected in oscillation mode. *Methods Enzymol.* **1997**, *276*, 307–326. [[CrossRef](#)] [[PubMed](#)]
35. Vagin, A.; Teplyakov, A. Molecular replacement with MOLREP. *Acta Crystallogr. D Biol. Crystallogr.* **2010**, *66*, 22–25. [[CrossRef](#)]
36. Nam, K.H. Room-Temperature Structure of Xylitol-Bound Glucose Isomerase by Serial Crystallography: Xylitol Binding in the M1 Site Induces Release of Metal Bound in the M2 Site. *Int. J. Mol. Sci.* **2021**, *22*, 3892. [[CrossRef](#)] [[PubMed](#)]
37. Casañal, A.; Lohkamp, B.; Emsley, P. Current developments in Coot for macromolecular model building of Electron Cryo-microscopy and Crystallographic Data. *Protein Sci.* **2020**, *29*, 1055–1064. [[CrossRef](#)]
38. Williams, C.J.; Headd, J.J.; Moriarty, N.W.; Prisant, M.G.; Videau, L.L.; Deis, L.N.; Verma, V.; Keedy, D.A.; Hintze, B.J.; Chen, V.B.; et al. MolProbity: More and better reference data for improved all-atom structure validation. *Protein Sci.* **2018**, *27*, 293–315. [[CrossRef](#)] [[PubMed](#)]
39. Krissinel, E.; Henrick, K. Inference of macromolecular assemblies from crystalline state. *J. Mol. Biol.* **2007**, *372*, 774–797. [[CrossRef](#)] [[PubMed](#)]
40. Larkin, M.A.; Blackshields, G.; Brown, N.P.; Chenna, R.; McGettigan, P.A.; McWilliam, H.; Valentin, F.; Wallace, I.M.; Wilm, A.; Lopez, R.; et al. Clustal W and Clustal X version 2.0. *Bioinformatics* **2007**, *23*, 2947–2948. [[CrossRef](#)]
41. Gouet, P.; Courcelle, E.; Stuart, D.I.; Metz, F. ESPript: Analysis of multiple sequence alignments in PostScript. *Bioinformatics* **1999**, *15*, 305–308. [[CrossRef](#)]
42. Henrick, K.; Collyer, C.A.; Blow, D.M. Structures of d-xylose isomerase from *Arthrobacter* strain B3728 containing the inhibitors xylitol and d-sorbitol at 2.5 Å and 2.3 Å resolution, respectively. *J. Mol. Biol.* **1989**, *208*, 129–157. [[CrossRef](#)]
43. Lee, M.; Rozeboom, H.J.; de Waal, P.P.; de Jong, R.M.; Dudek, H.M.; Janssen, D.B. Metal Dependence of the Xylose Isomerase from *Piromyces* sp. E2 Explored by Activity Profiling and Protein Crystallography. *Biochemistry* **2017**, *56*, 5991–6005. [[CrossRef](#)] [[PubMed](#)]
44. Allen, K.N.; Lavie, A.; Glasfeld, A.; Tanada, T.N.; Gerrity, D.P.; Carlson, S.C.; Farber, G.K.; Petsko, G.A.; Ringe, D. Role of the Divalent Metal Ion in Sugar Binding, Ring Opening, and Isomerization by D-Xylose Isomerase: Replacement of a Catalytic Metal by an Amino Acid. *Biochemistry* **2002**, *33*, 1488–1494. [[CrossRef](#)]
45. Katz, A.K.; Li, X.; Carrell, H.L.; Hanson, B.L.; Langan, P.; Coates, L.; Schoenborn, B.P.; Glusker, J.P.; Bunick, G.J. Locating active-site hydrogen atoms in d-xylose isomerase: Time-of-flight neutron diffraction. *Proc. Natl. Acad. Sci. USA* **2006**, *103*, 8342–8347. [[CrossRef](#)] [[PubMed](#)]
46. Hu, H.; Liu, H.; Shi, Y. The reaction pathway of the isomerization of d-xylose catalyzed by the enzyme d-xylose isomerase: A theoretical study. *Proteins* **1997**, *27*, 545–555. [[CrossRef](#)]
47. Kwon, S.; Ha, H.J.; Kang, Y.J.; Sung, J.H.; Hwang, J.; Lee, M.J.; Lee, J.H.; Park, H.H. Crystal structure of a novel putative sugar isomerase from the psychrophilic bacterium *Paenibacillus* sp. R4. *Biochem. Biophys. Res. Commun.* **2021**, *585*, 48–54. [[CrossRef](#)] [[PubMed](#)]
48. Bae, J.E.; Hwang, K.Y.; Nam, K.H. Structural analysis of substrate recognition by glucose isomerase in Mn²⁺ binding mode at M2 site in *S. rubiginosus*. *Biochem. Biophys. Res. Commun.* **2018**, *503*, 770–775. [[CrossRef](#)]
49. Xu, Y.; Nam, K.H. Xylitol binding to the M1 site of glucose isomerase induces a conformational change in the substrate binding channel. *Biochem. Biophys. Res. Commun.* **2023**, *682*, 21–26. [[CrossRef](#)]

Disclaimer/Publisher’s Note: The statements, opinions and data contained in all publications are solely those of the individual author(s) and contributor(s) and not of MDPI and/or the editor(s). MDPI and/or the editor(s) disclaim responsibility for any injury to people or property resulting from any ideas, methods, instructions or products referred to in the content.